

## Article

# Entropy Optimization on Axisymmetric Darcy–Forchheimer Powell–Eyring Nanofluid over a Horizontally Stretching Cylinder with Viscous Dissipation Effect

Muhammad Rooman <sup>1,2</sup>, Muhammad Asif Jan <sup>2</sup> , Zahir Shah <sup>1,\*</sup> , Narcisa Vrinceanu <sup>3,\*</sup> , Santiago Ferrández Bou <sup>4</sup> , Shahid Iqbal <sup>5</sup> and Wejdan Deebani <sup>6</sup> 

<sup>1</sup> Department of Mathematical Sciences, University of Lakki Marwat, Lakki Marwat 28420, Pakistan; roomankhan31@gmail.com

<sup>2</sup> Department of Mathematics, Kohat University of Science and Technology KUST, Kohat 26000, Pakistan; majan.math@gmail.com

<sup>3</sup> Department of Industrial Machines and Equipments, Faculty of Engineering, “Lucian Blaga” University of Sibiu, 10 Victoriei Boulevard, 550024 Sibiu, Romania

<sup>4</sup> Department of Mechanical and Materials Engineering, Higher Polytechnic School of Alcoy, Universitat Politècnica de València, 46022 Valencia, Spain; sferrand@mcm.upv.es

<sup>5</sup> Department of Physics, Albion College, Albion, MI 49224, USA; siqbali@albion.edu

<sup>6</sup> Department of Mathematics, College of Science & Arts, King Abdulaziz University, Rabigh 21911, Saudi Arabia; wdeebani@kau.edu.sa

\* Correspondence: zahir@ulm.edu.pk (Z.S.); vrinceanu.narcisai@ulbsibiu.ro (N.V.)



**Citation:** Rooman, M.; Jan, M.A.; Shah, Z.; Vrinceanu, N.; Ferrández Bou, S.; Iqbal, S.; Deebani, W. Entropy Optimization on Axisymmetric Darcy–Forchheimer Powell–Eyring Nanofluid over a Horizontally Stretching Cylinder with Viscous Dissipation Effect. *Coatings* **2022**, *12*, 749. <https://doi.org/10.3390/coatings12060749>

Academic Editor: Eduardo Guzmán

Received: 12 April 2022

Accepted: 26 May 2022

Published: 30 May 2022

**Publisher's Note:** MDPI stays neutral with regard to jurisdictional claims in published maps and institutional affiliations.



**Copyright:** © 2022 by the authors. Licensee MDPI, Basel, Switzerland. This article is an open access article distributed under the terms and conditions of the Creative Commons Attribution (CC BY) license (<https://creativecommons.org/licenses/by/4.0/>).

**Abstract:** The effect of entropy optimization on an axisymmetric Darcy–Forchheimer Powell–Eyring nanofluid flow caused by a horizontally permeable stretching cylinder, as well as non-linear thermal radiation, was investigated in this research work. The leading equations of the current problem were changed into ODEs by exhausting appropriate transformations. To deduce the reduced system, the numerical method bvp4c was used. The outcome of non-dimensional relevant factors on velocity, entropy, concentration, temperature, Bejan number, drag force, and Nusselt number is discussed and demonstrated using graphs and tables. It is perceived that, with a higher value of volume fraction parameter, the skin friction falls down. Likewise, it is found that the Nusselt number drops with enhancing the value of the volume fraction. Moreover, the result reveals that the entropy generation increases as the volume fraction, curvature parameter, and Brinkman number increase.

**Keywords:** heat transfer; stretching cylinder; nonlinear radiation; Powell–Eyring; nanofluid; porous medium; Darcy–Forchheimer

## 1. Introduction

It is a well-known fact that stretching flows have acquired a lot of attention because of their numerous applications. In industrial and mechanical engineering progressions (rubber and plastic sheets, cooling of electronic chips, glass blowing, metal spinning, production of glass fiber, liquid film crystallization during condensation, etc.), stretching surfaces are used extensively. In addition, various research of boundary layer flow in conjunction with a plane extending surface has already been carried out. However, research journals offer just a few experiments on horizontally stretching sheets with the axisymmetric flow. Crane [1] first studied the flow of viscous materials caused by a stretched sheet. Nadeem and Haq [2] investigated the convective flow of viscous nanoparticles using radiation beyond a stretched sheet. Ahmad et al. [3] explored power-law fluid in the occurrence of axisymmetric flow and heat transfer. Ariel [4] looked at the classic problem of an axisymmetric flow caused by a stretched sheet and gave perturbed, asymptotic, exact, and numerical solutions. Hsiao [5] investigated MHD heat transfer across a stretching surface utilizing Maxwell fluid flow by means of radiative and viscous dissipation properties.

Researchers are still interested in studying non-Newtonian fluids because they are more suitable for industrial areas such as power engineering, polymer solution industries, food engineering, and petroleum production. A linear association flanked by stress and rate of strain cannot be used to represent non-Newtonian fluids. Because of their various features, non-Newtonian fluids are much more complex than Newtonian fluids. Powell–Eyring fluids [6] are a type of non-Newtonian fluid with several compensations upon the power-law model, for example, they are built on liquid kinetic theory and behave Newtonian at both low and high shear rates. Patel et al. [7] used asymptotic boundary conditions to study a numeric solution of MHD Powell–Eyring fluid flow. Hayat et al. [8] discovered the radiative effects in electrically conducting Eyring–Powell fluid in three dimensions. Ara et al. [9] inspected the effect of radiation on Eyring–Powell fluid boundary layer flow across an exponentially shrinking sheet. Hayat et al. [10] showed boundary layer stagnation-point flow of Powell–Eyring fluid including dissolving heat transfer. In the existence of a double-stratified medium, Rehman et al. [11] numerically measured a flow study with heat generation/absorption influences of Powell–Eyring fluid mixed-convection flow around a stretching cylinder. According to Hayat et al. [12], these fluids had a variety of complicated features that provided them an edge and various applications over Newtonian fluids. Improvements in mud house renovation and the production of clay pots, gels, medical syrups, and fruit juices, such as Delmonte, yoghurt, Afya, and energy drinks are just a few of the benefits. Additionally, they are used in the production of pseudo-plastic fluids, paints, and medications in the pharmaceutical industry.

In thermodynamics, entropy is a key term. The concept of irreversibility is inextricably linked to the concept of entropy. Irreversibility is something that everyone instinctively understands. We may easily comprehend the irreversibility phenomenon by watching a movie in both forward and reverse sequences. Many progressive processes in ordinary life cannot be reversed, such as plastic deformation, pouring water into a glass, unrestrained fluid expansion, gas rising from a chimney, egg unscrambling, and so on. Originally, the term entropy was manipulated to define the loss of energy in numerous mechanical systems and heat engines that could not efficiently transform the energy into work. Many engineers and scientists are working hard in this modern period to find novel ways to control or limit the waste of valuable energy. This energy loss in thermodynamic systems can cause a lot of chaos. Using Bejan number and entropy creation, any system's efficiency can be boosted. Bejan [13] studied if heat transfer and flow mechanism abnormalities might be scrutinized in expressions of entropy formation. Many investigators have inspected entropy production results in heat flow and transmission to back up his claim. In a dissipative Blasius flow, But et al. [14] looked at entropy creation as well as radiative flux. Their findings show that as the heat radiation variable rises, entropy decreases. Entropy formation for mass and heat transmission over an isothermal medium was proposed by San and Laban [15]. Tamayol et al. [16] looked at how entropy affects heat transmission and fluid flow past a leaky material on a stretchy surface. Rashidi et al. [17] used the homotopy approach to entropy production in hydromagnetic flow across a spinning disk. Shit et al. [18] studied the irreversibility of hydromagnetic nanoparticle flow and heat transit on an exponentially speeded sheet. In the existence of radiative heat flux, convective boundary conditions, and MHD, the flow was explored. But and Ali [19] used a radially stretched surface to scrutinize the impact of a magnetic force on entropy formation in heat transfer and flow processes. Munawar et al. [20] deliberate the formation of entropy in viscid flow via an oscillated stretching cylinder. Khan et al. [21] used a radially stretched disk to evaluate the influence of entropy formation on Carreau nanofluid due to nonlinear thermal radiation.

Furthermore, nanotechnology is regarded as one of the most important conduits for the advancement in key manufacturing rebellion in our sector. Nanofluids are mostly employed due to their enhanced thermal properties. They are manipulated as coolants in heat transfer devices such as electronic cooling systems (such as flat plates), radiators, and heat exchangers. Nanofluid is made up of nanoparticles ranging in size from 1 to 100 nanometers. Choi and Eastman [22] were the first to propose the term “nanfluid”.

Iqbal et al. [23] used the Newtonian Carreau model to do a computational investigation of thin-film flow through a moving surface. Khan et al. [24] investigated the inspiration of Cattaneo–Christov heat flux on Maxwell nanofluid boundary layer hydromagnetic flow using the two-phase Buogirono model. Ali et al. [25] created the mathematical model of the unsteady and laminar couple stress nanofluid flow using engine oil and molybdenum disulphide nanomaterial as the base fluid and nanoparticles, respectively. They discovered that adding molybdenum disulphide nanoparticles to the base fluid improves the heat transfer rate of engine oil by up to 12.38 percent. Acharya et al. [26], investigated the effect of entropic production of a time-independent radioactive combination nanoliquid flowing through a slip spinning disk. Acharya et al. [27], used an entropy approach to evaluate mixed convection and radiation impacts in non-Newtonian-flowing fluid by a flexible cylinder. Verra Krishna and Chamkha [28] examined the impact of Hall and ion slip on the MHD convective flow of elastico-viscous fluid via a permeable channel between two rigidly rotating parallel plates. Takhar et al. [29], characterized the free stream of a vertically moving cylinder, as well as mass and heat transfer. A significant amount of noteworthy work has recently been accomplished [30–41].

Several scholars have looked into entropy propagation effects in the context of heat and mass transport on stretching surfaces. Although, there are just a few papers on the subject of entropy generation's impacts on inflow on a stretching disk. The consequences of entropy formation in Powell–Eyring nanofluid caused by mass and heat transport on a horizontally stretched disk are investigated in this article. The heat equation was modeled using several factors such as viscous dissipation, heat radiation, thermophoresis, and Brownian diffusion. The equations are numerically solved by the bvp4c method. The velocity, Bejan number, concentration, temperature, and entropy are all graphically explained.

## 2. Mathematical Formulation

The flow of Powell–Eyring nanofluid in a two-dimensional axisymmetric flow across a horizontally stretched sheet is assumed. We are using a system of cylindrical coordinates in which the  $z$ -axis, is chosen parallel to the cylinder's axis and the  $r$ -axis is chosen perpendicular to the cylindrical surface, as revealed in Figure 1. The cylinder is porous and continually stretches horizontally at  $u = u_\omega = \frac{U_0 z}{L}$ , where  $L$  is a characteristic length and  $U_0 > 0$ . Despite the fact that the moving fluid temperature is set to  $T_\infty$ , the cylindrical surface is kept at  $T_\omega$ , with the assumption that  $T_\omega > T_\infty$ . The Buongiorno model and nanofluid contain important slip mechanisms such as thermophoresis diffusion and Brownian motion. The velocity profile for the assumed flow is  $V = [w(r, z), 0, u(r, z)]$ .

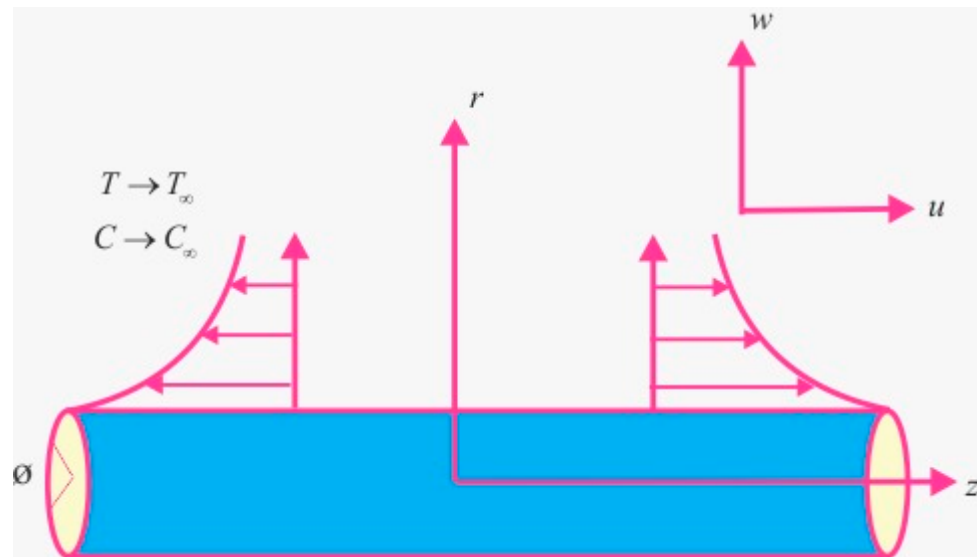


**Figure 1.** Sketch for the flow field.

The equations that govern the flow are as follows [10,11]

$$\frac{\partial(rw)}{\partial r} + \frac{\partial(ru)}{\partial z} = 0 \quad (1)$$

$$w\frac{\partial u}{\partial r} + u\frac{\partial u}{\partial z} = \frac{\mu_{nf}}{\rho_{nf}} \left( \frac{\partial^2 u}{\partial r^2} + \frac{1}{r} \frac{\partial u}{\partial r} \right) + \frac{1}{\rho_{nf}\beta c} \left( \frac{\partial^2 u}{\partial r^2} + \frac{1}{r} \frac{\partial u}{\partial r} \right) - \frac{1}{6\rho_{nf}\beta c^3} \left( \frac{1}{r} \left( \frac{\partial u}{\partial r} \right)^3 + 3 \left( \frac{\partial u}{\partial r} \right)^2 \left( \frac{\partial^2 u}{\partial r^2} \right) \right) - \frac{\mu_{nf}}{\rho_{nf}K} u - \frac{c_b}{\rho_{nf}\sqrt{K}} u^2 \quad (2)$$

$$w\frac{\partial T}{\partial r} + u\frac{\partial T}{\partial z} = \frac{k_{nf}}{(\rho c_p)_{nf}} \left( \frac{\partial^2 T}{\partial r^2} + \frac{1}{r} \frac{\partial T}{\partial r} \right) + \tau \left( D_B \frac{\partial C}{\partial r} \frac{\partial T}{\partial r} + \frac{D_T}{T_\infty} \left( \frac{\partial T}{\partial r} \right)^2 \right) + \frac{1}{(\rho c_p)_{nf}} \left( \mu_{nf} \left( \frac{\partial u}{\partial r} \right)^2 + \frac{1}{\beta c} \left( \frac{\partial u}{\partial r} \right)^2 - \frac{1}{6\beta c^3} \left( \frac{\partial u}{\partial r} \right)^4 \right) - \frac{1}{(\rho c_p)_{nf}} \frac{\partial}{\partial r} \left( -\frac{16\sigma^*}{3k^*k_{nf}} T^3 \frac{\partial T}{\partial r} \right) \quad (3)$$

$$w\frac{\partial C}{\partial r} + u\frac{\partial C}{\partial z} = D_B \left( \frac{\partial^2 C}{\partial r^2} + \frac{1}{r} \frac{\partial C}{\partial r} \right) + \frac{D_T}{T_\infty} \left( \frac{\partial^2 T}{\partial r^2} + \frac{1}{r} \frac{\partial T}{\partial r} \right) \quad (4)$$

With boundary conditions

$$u = u_\omega = \frac{U_0 z}{L}, w = 0, T = T_\omega, C = C_\omega \text{ at } r = R \\ u \rightarrow 0, T \rightarrow T_\infty, C \rightarrow C_\infty \text{ at } r \rightarrow \infty \quad (5)$$

Illustrations of the description of the various symbols are shown in Table 1. The fundamental equations can be transformed using the following transforms [21]:

$$\psi(r, z) = \sqrt{u_\omega \mu_f z} R f(\eta), \eta = \frac{r^2 - R^2}{2R} \sqrt{\frac{u_\omega}{\mu_f z}}, \theta(\eta) = \frac{T - T_\infty}{T_\omega - T_\infty}, \phi(\eta) = \frac{C - C_\infty}{C_\omega - C_\infty} \quad (6)$$

**Table 1.** A description of the multiple symbols that appear in the governing equations is illustrated.

Symbols	Description	Symbols	Description
$u, v, w$	Velocity in $r, \theta, z$ direction	$\beta, c$	Fluid parameter
$\mu_f$	Base fluid dynamic viscosity	$\mu_{nf}$	Nanofluid dynamic viscosity
$v_f$	Base fluid kinematic viscosity	$c_p$	Specific heat
$c_b$	Drag factor	$K$	Permeability of porous medium
$k_f$	Base fluid thermal conductivity	$k_{nf}$	Nanofluid thermal conductivity
$k_s$	Nanoparticles' thermal conductivity	$D_B$	Brownian motion
$\rho_f$	Base fluid density	$\rho_{nf}$	Nanofluid density
$L$	Characteristic length	$(\rho c_p)_f$	Heating capacity of base fluid
$(\rho c_p)_{nf}$	Heating capacity of nanofluid	$(\rho c_p)_s$	Heating capacity of nanoparticles
$T$	Temperature	$T_\infty$	Temperature at free stream
$k^*$	Absorption coefficient	$D_T$	Thermo-coefficient
$C$	Concentration	$C_\infty$	Ambient concentration

Equation (7) identifies the components of velocity

$$u = \frac{1}{r} \frac{\partial \psi(r, z)}{\partial r}, w = -\frac{1}{r} \frac{\partial \psi(r, z)}{\partial z} \quad (7)$$

The nanofluid expressions are given by [25]:

$$\left. \begin{aligned} \mu_{nf} &= \mu_f (1 - \phi)^{-2.5} \\ \rho_{nf} &= \rho_f (1 - \phi) + \phi \rho_s \\ (\rho c_p)_{nf} &= (\rho c_p)_f (1 - \phi) + \phi (\rho c_p)_s \\ k_{nf} &= k_f \left[ \frac{k_s + 2k_f - 2\phi(k_f - k_s)}{k_s + 2k_f + 2\phi(k_f - k_s)} \right] \end{aligned} \right\} \quad (8)$$

The base fluid and nanofluid dynamic viscosity are denoted by  $\mu_f$  and  $\mu_{nf}$ , respectively, where  $\phi$  signifies volume fraction.

The equation of incompressibility is fulfilled identically, whereas Equations (2)–(5) are reduced to

$$(1 + 2\eta\gamma)\left(\frac{1}{(1-\phi_1)^{2.5}} + \alpha\right)f''' - \lambda\alpha(1 + 2\eta\gamma)^2 f''^2 f''' + 2\gamma\left(\frac{1}{(1-\phi_1)^{2.5}} + \alpha\right)f'' - \frac{4}{3}\alpha\lambda\gamma(1 + 2\eta\gamma)f''^3 - \frac{\beta_0}{(1-\phi_1)^{2.5}}f' - F_rf'^2 + \left((1 - \phi_1) + \phi_1\frac{\rho_s}{\rho_f}\right)(ff'' - f'^2) = 0 \quad (9)$$

$$\begin{aligned} & \frac{k_{nf}/k_f}{Pr}((1 + 2\eta\gamma)\theta'' + \gamma\theta') + Ec(1 + 2\eta\gamma)\left(\left(\frac{1}{(1-\phi_1)^{2.5}} + \alpha\right)f''^2 - \frac{1}{3}\lambda\alpha(1 + 2\eta\gamma)f''^4\right) \\ & + \left((1 - \phi_1) + \phi_1\frac{(\rho c_p)_s}{(\rho c_p)_f}\right)(Nt(1 + 2\eta\gamma)\theta'^2 + Nb(1 + 2\eta\gamma)\theta'\phi' + f\theta') \\ & + \frac{Rd}{Prk_{nf}/k_f}(1 + 2\eta\gamma)\left((\theta(\theta_\omega - 1) + 1)^3\theta'' + 3(\theta(\theta_\omega - 1) + 1)^2(\theta_\omega - 1)\theta'^2\right) = 0 \end{aligned} \quad (10)$$

$$\frac{Nt}{Nb} \frac{1}{Sc} ((1 + 2\eta\gamma)\theta'' + \gamma\theta') + \frac{1}{Sc} ((1 + 2\eta\gamma)\phi'' + \gamma\phi') + f\phi' = 0 \quad (11)$$

$$\begin{aligned} f(0) &= 0, f'(0) = 1, \theta(0) = 1, \phi(0) = 1 \\ f'(\infty) &\rightarrow 0, \theta(\infty) \rightarrow 0, \phi(\infty) \rightarrow 0 \end{aligned} \quad (12)$$

where  $\gamma = \sqrt{\frac{v_f L}{U_0 R^2}}$  represents the curvature parameter,  $\alpha = \frac{1}{\mu_f \beta c}$  and  $\lambda = \frac{U_0^3 z^2}{2L^3 c^2 v_f}$  are fluid parameters,  $\beta_0 = \frac{Lv}{\rho_f U_0 K}$  represents the porosity parameter,  $F_r = \frac{c_b z}{\rho_f \sqrt{K}}$  is the inertia coefficient,  $Ec = \frac{u_\omega^2}{c_p(T_\omega - T_\infty)}$  is the Eckert number,  $Rd = \frac{16\sigma^* T_\infty^3}{3k^* k_f}$  denotes the radiation parameter,  $Pr = \frac{\mu c_p}{k_f}$  denotes the Prandtl number,  $\theta_\omega = \frac{T_\omega}{T_\infty}$  is the temperature ratio,  $S_c = \frac{V_f}{D_B}$  is the Schmidt number,  $Nt = \frac{\tau D_B(T_\omega - T_\infty)}{v_f}$  and  $Nb = \frac{\tau D_B(C_\omega - C_\infty)}{v_f}$  represent the thermophoresis and Brownian diffusion parameters, respectively.

### Skin Friction and Nusselt Number

The following are the definitions of the skin friction and the local Nusselt number:

$$c_f = \frac{\tau_\omega}{\rho_f u_\omega^2}, N_u = \frac{z q_\omega}{k_f(T_f - T_\infty)} \quad (13)$$

where  $\tau_\omega$  and  $q_\omega$  are the surface shear stress and heat flux, respectively. These are defined as:

$$\tau_\omega = \left[ \left( \mu_{nf} + \frac{1}{\beta c} \right) \left( \frac{\partial u}{\partial r} \right) - \frac{1}{6\beta c^3} \left( \frac{\partial u}{\partial r} \right)^3 \right]_{r=R}, q_\omega = - \left( k_{nf} + \frac{16\sigma^* T_\infty^3}{3k^*} \right) \left( \frac{\partial T}{\partial r} \right)_{r=R} \quad (14)$$

In dimensionless form, the skin friction and Nusselt number are:

$$C_f Re_z^{1/2} = \left( \frac{1}{(1 - \phi_1)^{2.5}} + \alpha \right) f''(0) - \frac{\lambda}{3} \alpha (f''(0))^3, N_u Re_z^{-1/2} = - \left( \frac{k_{nf}}{k_f} + Rd \right) \theta'(0) \quad (15)$$

### 3. Entropy Optimization and Bejan Number

There are three causes of entropy Optimization in the current problem. Heat transport, viscous dissipation, and mass diffusion all generate entropy. The entropy equation is written as follows [18,21]:

$$\begin{aligned} S_g &= \frac{k_{nf}}{T_\infty^2} \left( 1 + \frac{16\sigma^* T_\infty^3}{3k^* k_{nf}} \right) \left( \frac{\partial T}{\partial r} \right)^2 + \frac{1}{T_\infty} \left( \mu_{nf} \left( \frac{\partial u}{\partial r} \right)^2 + \frac{1}{\beta c} \left( \frac{\partial u}{\partial r} \right)^2 - \frac{1}{6\beta c^3} \left( \frac{\partial u}{\partial r} \right)^4 \right) \\ &+ \frac{RD}{T_\infty} \left( \frac{\partial T}{\partial r} \frac{\partial C}{\partial r} \right) + \frac{RD}{C_\infty} \left( \frac{\partial C}{\partial r} \right)^2 \end{aligned} \quad (16)$$

By using the typical entropy generation rate to convert Equation (16) to dimensionless form, we obtain:

$$N_G = \left( \frac{k_{nf}}{k_f} + Rd(\theta(\theta_\omega - 1) + 1)^3 \right) (1 + 2\eta\gamma)\alpha_1\theta'^2 + L_1(1 + 2\eta\gamma)\theta'\phi' + L_1(1 + 2\eta\gamma)\frac{\alpha_2}{\alpha_1}\phi'^2 + Br(1 + 2\eta\gamma) \left( \left( \frac{1}{(1-\phi_1)^{2.5}} + \alpha \right) f''^2 - \frac{1}{3}\alpha\lambda f''^4 \right) \quad (17)$$

where  $N_G = \frac{S_g}{S_0} = \frac{S_g}{k_f U_0 (T_\omega - T_\infty) / T_\infty \mu_f L}$  denotes the total entropy production,  $\alpha_1 = \frac{T_\omega - T_\infty}{T_\infty}$  and  $\alpha_2 = \frac{C_\omega - C_\infty}{C_\infty}$  are the temperature ratio and concentration ratio variables, respectively, and  $Br = \frac{\mu_f U_0^2 z^2}{k_f L^2 (T_\omega - T_\infty)}$  and  $L_1 = \frac{RD(C_\omega - C_\infty)}{k_f}$  are Brinkman number and diffusion parameter, respectively.

Equation (17) can be written using the pattern shown below:

$$N_G = N_H + N_f + N_m \quad (18)$$

Here,  $N_H$  represents entropy production because of heat transmission,  $N_f$  represents entropy production because of fluid friction, and  $N_m$  represents entropy production. The Bejan number is defined as:

$$Be = \frac{N_H + N_m}{N_G} \quad (19)$$

$$Be = \frac{\left( \frac{k_{nf}}{k_f} + R(\theta(\theta_\omega - 1) + 1)^3 \right) (1 + 2\eta\gamma)\theta'^2\alpha_1 + L(1 + 2\eta\gamma)\theta'\phi' + L(1 + 2\eta\gamma)\frac{\alpha_2}{\alpha_1}\phi'^2}{\left( \left( \frac{k_{nf}}{k_f} + Rd(\theta(\theta_\omega - 1) + 1)^3 \right) (1 + 2\eta\gamma)\alpha_1\theta'^2 + Br(1 + 2\eta\gamma) \left( \left( \frac{1}{(1-\phi_1)^{2.5}} + \alpha \right) f''^2 - \frac{1}{3}\alpha\lambda f''^4 \right) \right. \\ \left. + L_1(1 + 2\eta\gamma)\theta'\phi' + L_1(1 + 2\eta\gamma)\frac{\alpha_2}{\alpha_1}\phi'^2 \right)} \quad (20)$$

#### 4. Numerical Method

The solution mechanism for the currently constructed model is computed in this part manipulating the bvp4c technique (shooting scheme). The bvp4c technique (shooting scheme) in the MATLAB tool is used to solve the ODEs (7)–(11) via (12) numerically. First, we transform a higher-order system to a first-order system for this technique. To accomplish this, we follow the steps below:

$$\begin{aligned} f &= y_1, f' = y_2, f'' = y_3, f''' = y'_3 \\ \theta &= y_4, \theta' = y_5, \theta'' = y'_5 \\ \phi &= y_6, \phi' = y_7, \phi'' = y'_7 \end{aligned} \quad (21)$$

$$y'_3 = \frac{\left( \frac{4}{3}\alpha\lambda\gamma(1 + 2\eta\gamma)y_3^3 - 2\gamma \left( \frac{1}{(1-\phi_1)^{2.5}} + \alpha \right) y_3 \right. \\ \left. + \frac{\beta_0}{(1-\phi_1)^{2.5}}y_2 + F_r y_2^2 - \left( (1 - \phi_1) + \phi_1 \frac{\rho_s}{\rho_f} \right) (y_1 y_3 - y_2^2) \right)}{(1 + 2\eta\gamma) \left( \frac{1}{(1-\phi_1)^{2.5}} + \alpha \right) - \lambda\alpha(1 + 2\eta\gamma)^2 y_3^2} \quad (22)$$

$$y'_5 = \frac{\left( E_c(1 + 2\eta\gamma) \left( \frac{1}{3}\lambda\alpha(1 + 2\eta\gamma)y_3^4 - \left( \frac{1}{(1-\phi_1)^{2.5}} + \alpha \right) y_3^2 \right) - \frac{k_{nf}/k_f}{Pr} \gamma y_5 \right. \\ \left. - \left( (1 - \phi_1) + \phi_1 \frac{(\rho c_p)_s}{(\rho c_p)_f} \right) (Nt(1 + 2\eta\gamma)y_5^2 + Nb(1 + 2\eta\gamma)y_5 y_7 + y_1 y_5) \right. \\ \left. - 3 \frac{Rd}{Pr k_{nf}/k_f} (1 + 2\eta\gamma)(y_4(\theta_\omega - 1) + 1)^2 (\theta_\omega - 1) y_5^2 \right)}{\frac{k_{nf}/k_f}{Pr} (1 + 2\eta\gamma) + \frac{Rd}{Pr k_{nf}/k_f} (1 + 2\eta\gamma)(y_4(\theta_\omega - 1) + 1)^3} \quad (23)$$

$$y'_7 = \frac{-\frac{Nt}{Nb}((1 + 2\eta\gamma)y'_5 + \gamma y_5) - (\gamma y_7) - Sc y_1 y_7}{(1 + 2\eta\gamma)} \quad (24)$$

with

$$\begin{aligned} y_1(0) &= 0, y_2(0) = 1, y_4(0) = 1, y_6(0) = 1 \\ y_2(\infty) &\rightarrow 0, y_4(\infty) \rightarrow 0, y_6(\infty) \rightarrow 0 \end{aligned} \quad (25)$$

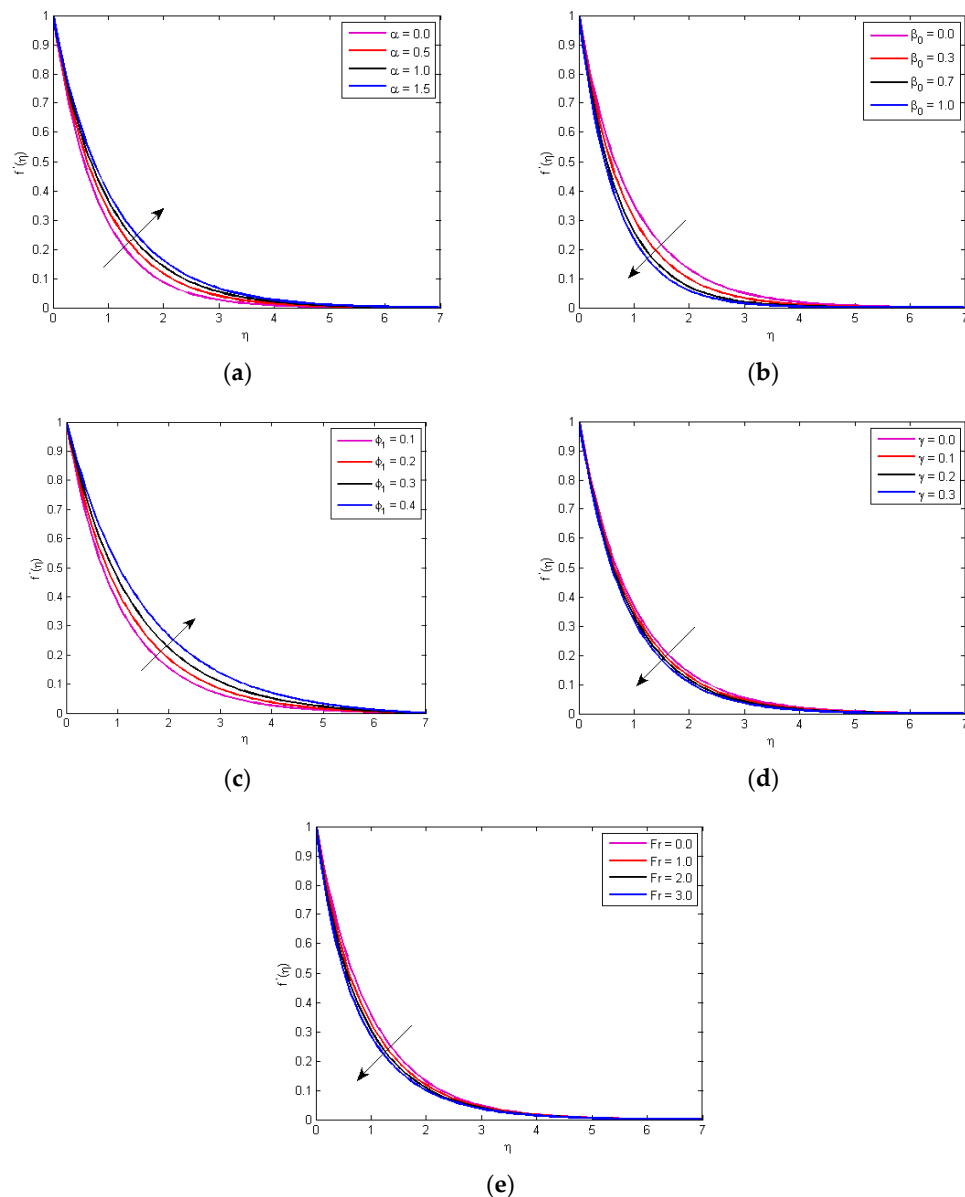
## 5. Results and Discussions

This section's focus is on examining the effects of velocity, temperature, concentration profile, entropy generation, and Bejan number. The influence of fluid parameter  $\alpha$ , porosity parameter  $\beta_0$ , volume fraction  $\phi_1$ , curvature parameter  $\gamma$ , and inertia coefficient  $Fr$  on fluid velocity is examined in Figure 2a–e. The effect of fluid parameter  $\alpha$  on the velocity profile is presented in Figure 2a. With the higher value of  $\alpha$ , the fluid velocity and boundary layer thickness increase. In reality, as  $\alpha$  increases, the viscosity of the fluid declines, resulting in an improvement in the velocity profile. The impression of the porosity factor  $\beta_0$  on the velocity profile of Powell–Eyring nanofluid is shown in Figure 2b. The velocity of the nanofluid declines when permeability of the fluid rises, which is in line with authenticity. Moreover, the permeability of the border has no consequence on the fluid velocity as we move away from it. The impact of volume fraction  $\phi_1$  on velocity profile is plotted in Figure 2c. By raising the volume fraction, the Powell–Eyring nanofluid velocity decreases. The science here seems to be that when the volume fraction increases, the flow becomes more vicious, resulting in friction forces that slow the nanofluid velocity. The feature of the curvature parameter  $\gamma$  on the velocity profile is presented in Figure 2d. As  $\gamma$  goes up, the fluid velocity shrinks at the surface and escalates further from the cylinder, according to the results. In reality, as the curvature parameter is increased, the cylinder's radius decreases. As a result, the cylinder's contact surface with the fluid lowers, providing less confrontation to fluid motion. Consequently, the velocity profile rises. The impression of inertia coefficient  $Fr$  on the velocity profile is shown in Figure 2e. The velocity profile drops as the inertia coefficient rises.

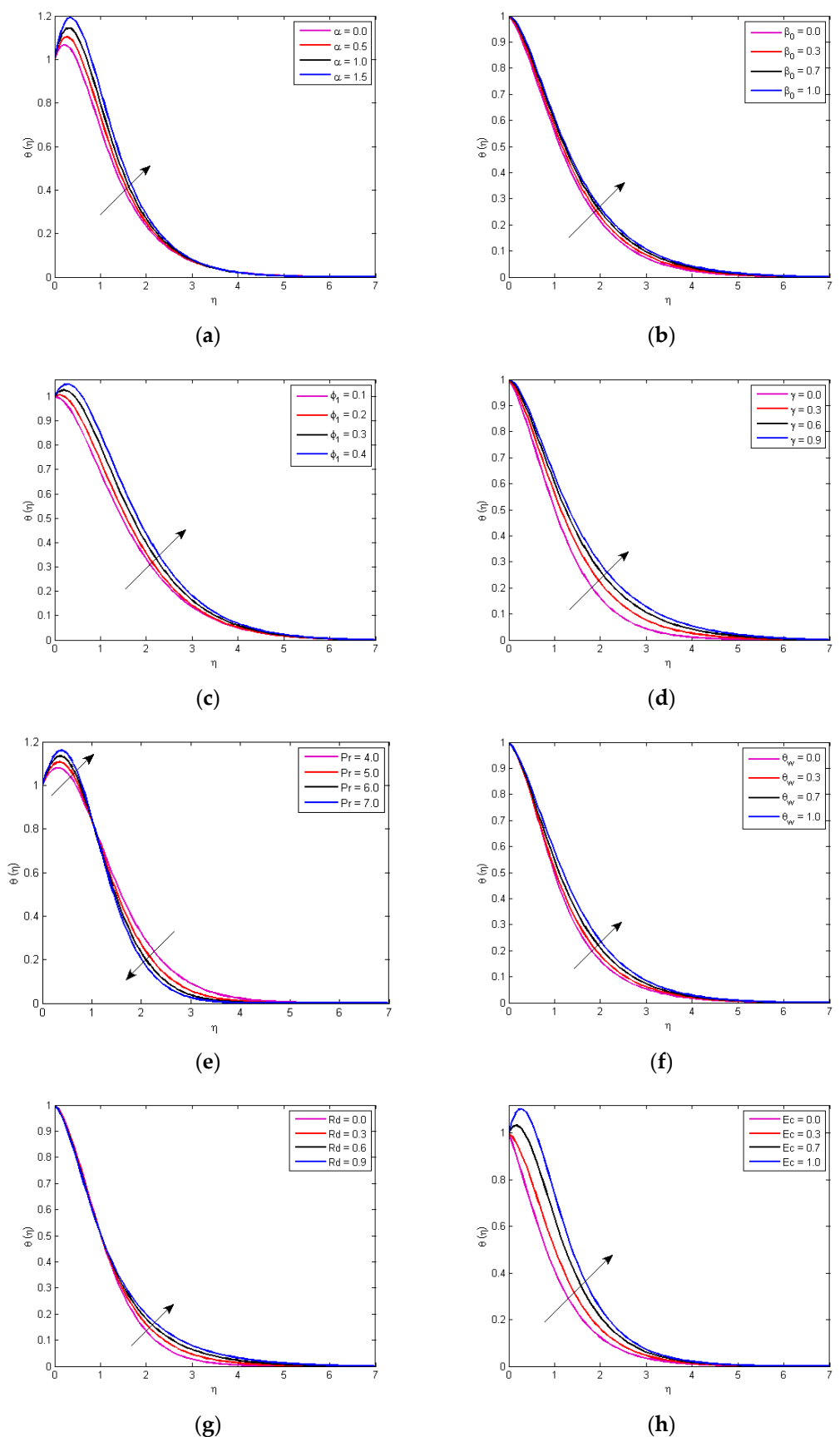
The impact of temperature profile  $\theta(\eta)$  against relevant flow parameters, such as fluid parameter  $\alpha$ , porosity parameter  $\beta_0$ , curvature parameter  $\gamma$ , Prandtl number  $Pr$ , temperature ratio  $\theta_\omega$ , thermal radiation  $Rd$ , Eckert number  $Ec$ , thermophoresis constraint  $Nt$ , and Brownian motion constraint  $Nb$ , are depicted in Figure 3a–j. Figure 3a signifies the inspiration of the fluid constraint  $\alpha$  on the temperature profile. Higher  $\alpha$  values result in a lower temperature profile, according to the findings. The viscosity of the thermal boundary layer continues to shrink, as the higher value of fluid parameter  $\alpha$  viscosity of the fluid decreases.

Accordingly, the temperature profile declines. The variation in temperature profile with  $\eta$ , over a range of the porous parameter  $\beta_0$  is shown in Figure 3b. This illustration clearly demonstrates that the heat distribution is a weak function of  $\beta_0$  and that it changes little when it passes through the thermal boundary layer. Therefore, increasing  $\beta_0$  causes a modest thickening of the thermal boundary layer. The outcome of volume fraction parameter  $\phi_1$  on the temperature profile is depicted in Figure 3c. It is observed that the increasing volume fraction raises the temperature profile. The science behind this mounting temperature pattern is because the temperature rises as the smash flanked by the molecules of the Powell–Eyring nanofluid rises. Figure 3d exhibits the impressions of the curvature constraint on the temperature profile, with temperature showing an increasing trend via  $\gamma$ . As  $\gamma$  increases, the surface contact area exposed to fluid particles decreases, resulting in less resistance for particles and an increase in their average velocity. The temperature rises because the Kelvin temperature is expressed by an average kinetic energy. The characteristics of the Prandtl number  $Pr$  on the temperature distribution are exposed in Figure 3e. The temperature profile and thickness of the thermal boundary layer are found to diminish as the Prandtl number rises. It connects thermal diffusivity to momentum diffusivity. Accordingly, a higher Prandtl number correlates to a reduced thermal diffusivity; consequently, temperature distribution rises up before dropping down. Figure 3f depicts the effects of temperature ratio  $\theta_\omega$  on the temperature distribution. It has been realized that advanced temperature ratio enhances the temperature distribution. Figure 3g depicts the

behavior of the radiation parameter  $Rd$  on a temperature profile. For bulky levels of the radiation parameter, temperature and the accompanying boundary layer thickness rise. Higher values of the radiation parameter reduce the mean absorption coefficient, resulting in an upturn in the temperature distribution. Figure 3h depicts the difference in fluid temperature caused by the change in Eckert number  $Ec$ . The figure depicts how the fluid temperature rises as the value of  $Ec$  rises. This happens since frictional heating produces heat in the fluid as the value of  $Ec$  rises. Physically, the Eckert number is explained as the ratio of kinetic energy to the difference in specific enthalpy flanked by the wall and the fluid. As a result of the effort exerted against the viscous fluid pressures, an upsurge in Eckert number converts kinetic energy into internal energy. As a result, as  $Ec$  rises, the fluid's temperature rises. As shown in Figure 3i, the thermophoresis parameter  $Nt$  has an outcome on the temperature. The graph shows that as the number of thermophoresis parameters  $Nt$  increases, so does the temperature. The temperature of the fluid rises as the temperature variance amid the surface and ambient heat grows. The stimulus of the Brownian motion  $Nb$  on the temperature is revealed in Figure 3j. This graph shows that augmented  $Nb$  raises the temperature.



**Figure 2.** Velocity profile variation for distinct values of (a) is  $\alpha$ , (b) is  $\beta_0$ , (c) is  $\phi_1$ , (d) is  $\gamma$ , (e) is  $Fr$ .

**Figure 3. Cont.**

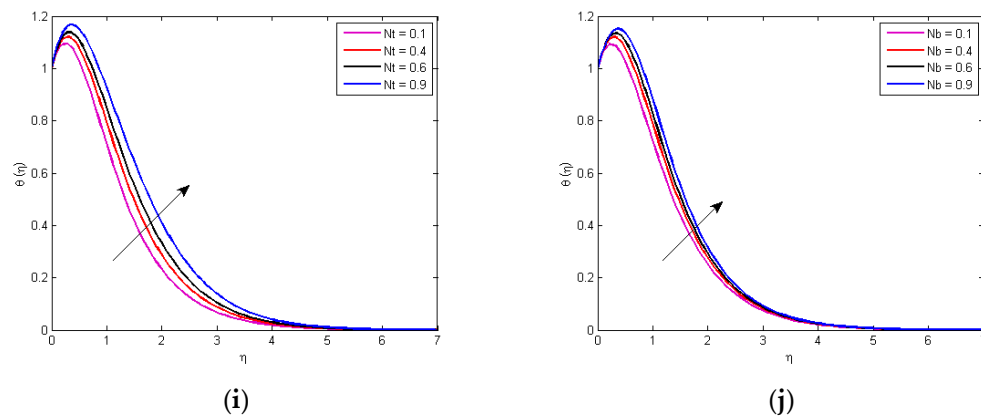


**Figure 3.** Temperature profile variation for distinct values of (a) is  $\alpha$ , (b) is  $\beta_0$ , (c) is  $\phi_1$ , (d) is  $\gamma$ , (e) is  $Pr$ , (f) is  $\theta_\omega$ , (g) is  $Rd$ , (h) is  $Ec$ , (i) is  $Nt$ , (j) is  $Nb$ .

The consequence of significant flow parameters such as the fluid parameter  $\alpha$ , curvature parameter  $\gamma$ , the Schmidt number  $Sc$ , and volume fraction  $\phi_1$  on the concentration profile  $\alpha$  are exposed in Figure 4a–d. Figure 4a demonstrates the influence of fluid parameter  $\alpha$  on concentration distribution  $\phi(\eta)$ . It is detected that the concentration profile declines by rising the value of  $\alpha$ . The inspiration of curvature constraint  $\gamma$  on the concentration profile  $\phi(\eta)$  is shown in Figure 4b. Proof is provided through  $\gamma$  rising along with the fluid concentration and the thickness of the resulting boundary layer. The impacts of Schmidt number  $Sc$  and volume fraction  $\phi_1$  on the distribution of concentrations are depicted in Figure 4c,d, respectively. As can be observed in both of these diagrams, the concentration distribution diminishes for substantial values of  $Sc$  and  $\phi_1$ . The reason for this phenomenon is that viscous forces increase as the concentration slows down.  $Sc$  is the ratio of mass diffusion to viscous forces at each end of the scale. As  $Sc$  increases, viscous forces grow and mass diffusion declines, causing the concentration distribution to decrease.

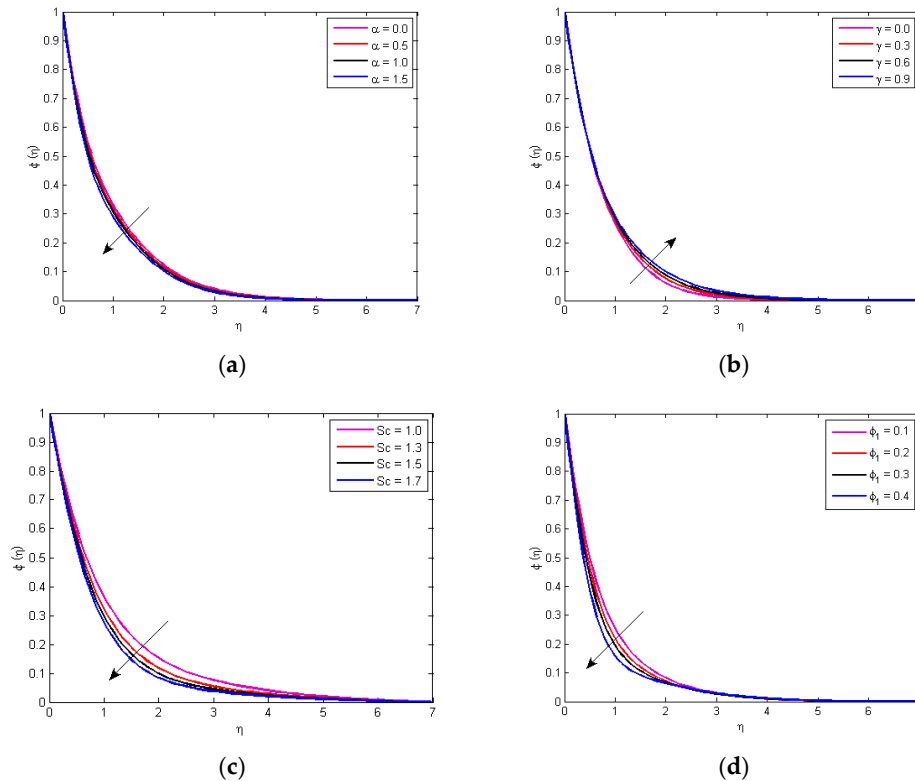


**Figure 4.** Concentration profile variation for distinct values of (a) is  $\alpha$ , (b) is  $\gamma$ , (c) is  $Sc$ , (d) is  $\phi_1$ .

The behavior of entropy optimization and Bejan number is shown in Figures 5 and 6, respectively, for various parameters such as porosity parameter  $\beta_0$ , volume fraction  $\phi_1$ , curvature parameter  $\gamma$ , and Brinkman number  $Br$ . Figures 5a and 6a show the nature of entropy formation and Bejan number for the rising porosity parameter  $\beta_0$ . As the values of porosity parameter  $\beta_0$  upsurge, the values of entropy generation escalations near the wall slightly decrease; the Bejan number, on the other hand, exhibits the opposite pattern. As the porosity parameter tends to oppose the fluid flow, as a result, it increases the rate of total entropy formation. The influence of nanoparticles' volume fraction parameter  $\phi_1$  on entropy production and Bejan number is exposed in Figures 5b and 6b. These figures show that entropy production increases, while Bejan number drops with an escalation in volume fraction parameter  $\phi_1$ . The increase in thermal conductivity and temperature of nanofluid caused by nanoparticles is directly related to this phenomenon. Figures 5c and 6c show the stimuli of the curvature parameter on entropy formation and Bejan number, respectively. As  $\gamma$  upturns, the value of Bejan number and entropy generation increases, because less resisting force is offered when the contact surface of a cylinder with particles is reduced. This allows for more nanoparticle movement, increasing the rate of entropy formation. As a result, more curved bodies produce more entropy. Figures 5d and 6d show the nature of entropy formation and Bejan number for the rising Brinkman number  $Br$ . The outcomes of entropy formation and Bejan number are utterly opposite when Brinkman number  $Br$  is changed. Entropy production increases as the Brinkman number increases, as shown in Figure 5d. The ratio of heat creation via viscous heating transition for conduction is known as the Brinkman number. More heat is created in the system to reimburse for increasing Brinkman number. As a result, the overall system's level of disturbance grows. For a high Brinkman number  $Br$ , Figure 6d shows the exact opposite characteristics.

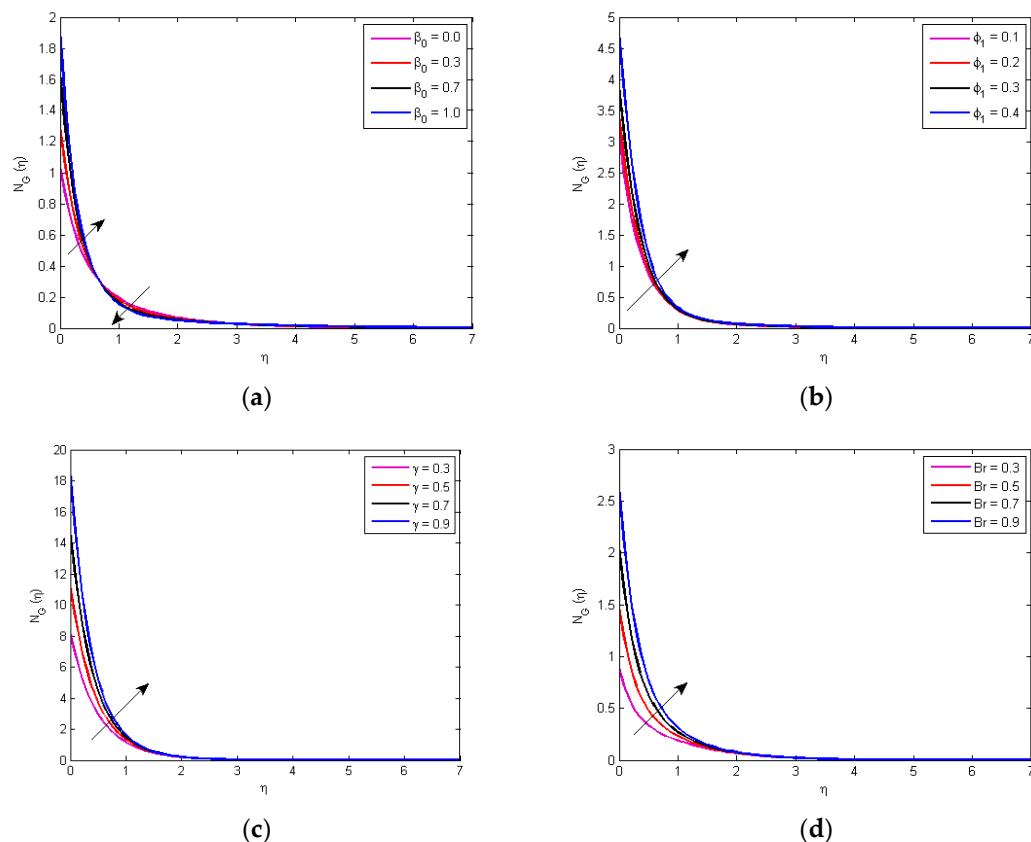


**Figure 5.** Entropy optimization variation for distinct values of (a) is  $\beta_0$ , (b) is  $\phi_1$ , (c) is  $\gamma$ , (d) is  $Br$ .

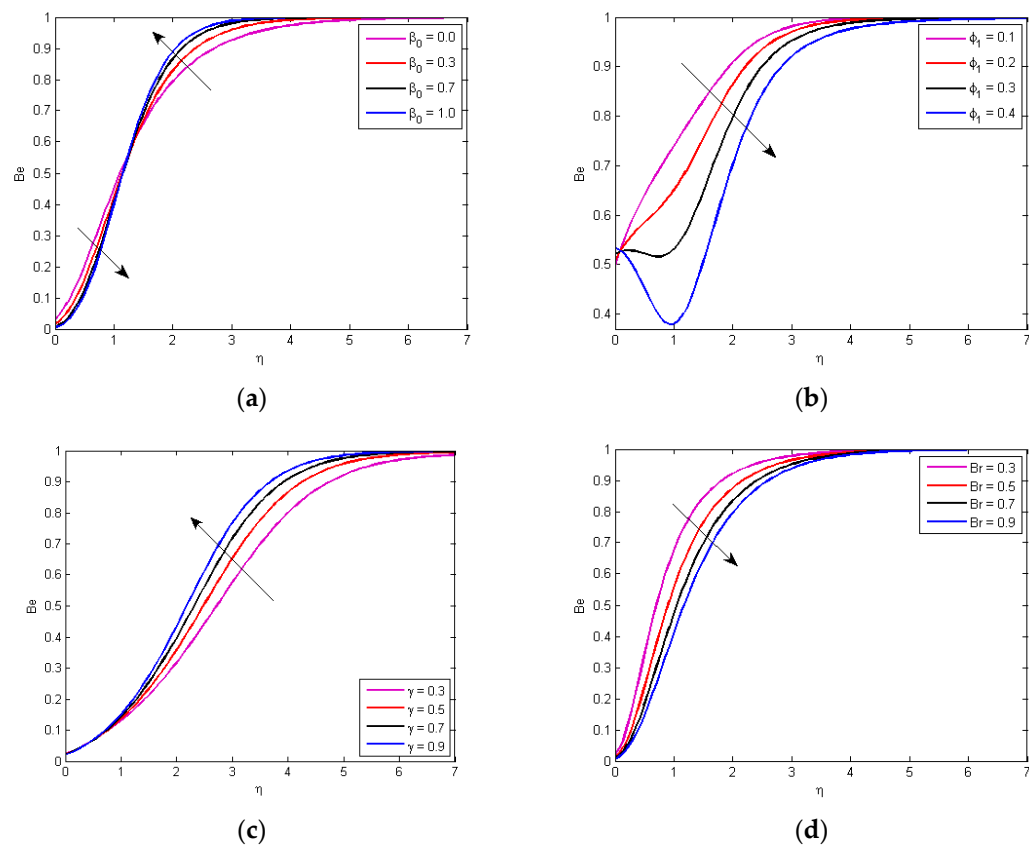


**Figure 6.** Bejan number variation for distinct values of (a) is  $\beta_0$ , (b) is  $\phi_1$ , (c) is  $\gamma$ , (d) is  $Br$ .

Table 2 indicates how the numerous constraints affect the skin friction. It is determined that skin friction coefficient decreases for large values of the volume fraction, fluid parameter, porosity parameter, curvature parameter, and inertia coefficient. Table 3 indicates the numeric data of the Nusselt number for a variety of constraints. It is determined that Nusselt number decreases for large values of the volume fraction, fluid parameter, porosity parameter, and temperature ratio, whereas it upsurges for superior values of the curvature parameter. Table 4 compares the numeric values of skin fraction with the previous result. Both outcomes are noticed to be highly congruent.

**Table 2.** The skin friction coefficient variation for numerous values of  $\phi_1$ ,  $\alpha$ ,  $\beta_0$ ,  $\gamma$ , and  $Fr$ .

$\phi_1$	$\alpha$	$\beta_0$	$\gamma$	$Fr$	$C_f Re_z^{1/2}$
0.1	-	-	-	-	-2.463269
0.2	-	-	-	-	-2.919301
0.3	-	-	-	-	-3.6675
0.1	0.1	-	-	-	-2.002416
-	0.3	-	-	-	-2.223522
-	0.5	-	-	-	-2.463269
-	-	0.1	-	-	-2.272982
-	-	0.3	-	-	-2.368182
-	-	0.5	-	-	-2.463269
-	-	-	0.1	-	-1.893775
-	-	-	0.3	-	-2.045572
-	-	-	0.5	-	-2.186751
-	-	-	-	0.1	-1.948242
-	-	-	-	0.5	-2.045572
-	-	-	-	0.9	-2.138431

**Table 3.** The variation in Nusselt number for numerous values of  $\phi_1$ ,  $\alpha$ ,  $\beta_0$ ,  $\gamma$ , and  $\theta_\omega$ .

$\phi_1$	$\alpha$	$\beta_0$	$\gamma$	$\theta_\omega$	$N_u \text{Re}_z^{-1/2}$
0.1	-	-	-	-	0.416374
0.2	-	-	-	-	0.413638
0.3	-	-	-	-	0.3887
-	0.1	-	-	-	0.449055
-	0.3	-	-	-	0.43289
-	0.5	-	-	-	0.416374
-	-	0.1	-	-	0.441787
-	-	-	-	-	0.428625
-	-	-	-	-	0.416374
-	-	-	0.1	-	0.330731
-	-	-	0.3	-	0.357808
-	-	-	0.5	-	0.380167
-	-	-	-	0.1	0.419923
-	-	-	-	0.3	0.418526
-	-	-	-	0.5	0.409504
-	-	-	-	-	-
-	-	-	-	-	-

**Table 4.** Comparison of  $f''(0)$  skin friction values for several fluid parameter  $\alpha$  values.

$\alpha$	Present Result	Hayat et al. [12]
0.2	-0.7749406	-0.91287
0.4	-0.7282394	-0.84516
0.6	-0.6891753	-0.79057
0.8	-0.6558923	-0.74536
1.0	-0.6270961	-0.70711

## 6. Conclusions

In this research, an entropy generation interpretation for axisymmetric flow of Powell-Eyring nanofluid via a horizontal porous stretching cylinder was performed. By using a similarity variable transformation system, the nonlinear equation describing the flow problem is changed to nonlinear ODEs, which are then solved using bvp4c. The impacts of several factors in the model problem on velocity, temperature, concentration, entropy optimization, Bejan number, drag force, and Nusselt number are analyzed. The following conclusions were derived from the study's findings:

- It is indicated that with growing value of fluid parameter  $\alpha$ , velocity increased, while with rising values of porosity parameter  $\beta_0$ , the volume fraction  $\phi_1$ , curvature parameter  $\gamma$ , and inertia coefficient  $Fr$  velocity profile declined.
- The temperature declined with the mounting value of fluid parameter  $\alpha$ , whereas it increased with increasing values of the porosity parameter  $\beta_0$ , volume fraction  $\phi_1$ , curvature parameter  $\gamma$ , temperature ratio  $\theta_\omega$ , thermal radiation  $Rd$ , Eckert number  $Ec$ , thermophoresis parameter  $Nt$ , and Brownian motion  $Nb$ . It is noted that the temperature of the fluid rose up and then dropped down when we increased the Prandtl number.
- The concentration profile declined with rising values of fluid parameter  $\alpha$ , curvature parameter  $\gamma$ , the Schmidt number  $Sc$ , and volume fraction  $\phi_1$ .
- Entropy optimization rose up for the values of volume fraction  $\phi_1$ , curvature parameter  $\gamma$ , and Brinkman number  $Br$ , whereas for the rising value of porosity parameter  $\beta_0$ , entropy optimization first increased and then decreased.
- Bejan number decayed down for greater  $\phi_1$  and Brinkman number, while for a higher value of curvature parameter, Bejan number rose up. It is indicated that if we increased the porosity parameter  $\beta_0$ , Bejan number decayed down first and then rose up.

- It is concluded that skin friction decreased for a large number of volume fraction, fluid parameter, porosity parameter, curvature parameter, and inertia coefficient, whereas Nusselt number decreased for a cumulative number of volume fraction, fluid parameter, porosity parameter, and temperature ratio, whereas it rose for a cumulative number of curvature parameter.

**Author Contributions:** Conceptualization, M.R. and N.V.; methodology, Z.S. and M.A.J.; software, M.R.; validation, N.V. and W.D.; formal analysis, S.F.B. and S.I.; investigation, Z.S. and M.R.; resources, N.V.; data curation, W.D.; writing—original draft preparation, M.R.; writing—review and editing, Z.S., N.V. and S.I.; visualization, W.D.; supervision, M.A.J. and Z.S.; project administration, N.V. and S.F.B.; funding acquisition, N.V. and S.F.B. All authors have read and agreed to the published version of the manuscript.

**Funding:** The project was financed by Lucian Blaga University of Sibiu and Hasso Plattner Foundation research Grants LBUS-IRG-2021-07.

**Institutional Review Board Statement:** Not applicable.

**Informed Consent Statement:** Not applicable.

**Data Availability Statement:** The data that support the findings of this study are available from the corresponding author upon reasonable request.

**Conflicts of Interest:** The authors declare no conflict of interest.

## References

1. Crane, L.J. Flow past a stretching plate. *Z. Angew. Math. Phys. ZAMP* **1970**, *21*, 645–647. [[CrossRef](#)]
2. Nadeem, S.; Ul Haq, R. Effect of thermal radiation for magnetohydrodynamic boundary layer flow of a nanofluid past a stretching sheet with convective boundary conditions. *J. Comput. Theor. Nanosci.* **2014**, *11*, 32–40. [[CrossRef](#)]
3. Ahmed, J.; Mahmood, T.; Iqbal, Z.; Shahzad, A.; Ali, R. Axisymmetric flow and heat transfer over an unsteady stretching sheet in power law fluid. *J. Mol. Liq.* **2016**, *221*, 386–393. [[CrossRef](#)]
4. Ariel, P.D. Axisymmetric flow of a second grade fluid past a stretching sheet. *Int. J. Eng. Sci.* **2001**, *39*, 529–553. [[CrossRef](#)]
5. Hsiao, K.L. Combined electrical MHD heat transfer thermal extrusion system using Maxwell fluid with radiative and viscous dissipation effects. *Appl. Therm. Eng.* **2017**, *112*, 1281–1288. [[CrossRef](#)]
6. Powell, R.E.; Eyring, H. Mechanisms for the Relaxation Theory of Viscosity. *Nature* **1944**, *154*, 427–428. [[CrossRef](#)]
7. Patel, M.; Timol, M.G. Numerical treatment of Powell-Eyring fluid flow using Method of Satisfaction of Asymptotic Boundary Conditions (MSABC). *Appl. Numer. Math.* **2009**, *59*, 2584–2592. [[CrossRef](#)]
8. Hayat, T.; Awais, M.; Asghar, S. Radiative effects in a three-dimensional flow of MHD Eyring-Powell fluid. *J. Egypt. Math. Soc.* **2013**, *21*, 379–384. [[CrossRef](#)]
9. Ara, A.; Khan, N.A.; Khan, H.; Sultan, F. Radiation effect on boundary layer flow of an Eyring–Powell fluid over an exponentially shrinking sheet. *Ain Shams Eng. J.* **2014**, *5*, 1337–1342. [[CrossRef](#)]
10. Hayat, T.; Farooq, M.; Alsaedi, A.; Iqbal, Z. Melting heat transfer in the stagnation point flow of powell-eyring fluid. *J. Thermophys. Heat Transf.* **2013**, *27*, 761–766. [[CrossRef](#)]
11. Rehman, K.U.; Malik, M.Y.; Salahuddin, T.; Naseer, M. Dual stratified mixed convection flow of Eyring-Powell fluid over an inclined stretching cylinder with heat generation/absorption effect. *AIP Adv.* **2016**, *6*, 075112. [[CrossRef](#)]
12. Hayat, T.; Hussain, Z.; Farooq, M.; Alsaedi, A. Magnetohydrodynamic flow of powell-eyring fluid by a stretching cylinder with Newtonian heating. *Therm. Sci.* **2018**, *22*, 371–382. [[CrossRef](#)]
13. Bejan, A. A Study of Entropy Generation in Fundamental Convective Heat Transfer. *J. Heat Transfer* **1979**, *101*, 718–725. [[CrossRef](#)]
14. Butt, A.S.; Munawar, S.; Ali, A.; Mehmood, A. Entropy generation in the Blasius flow under thermal radiation. *Phys. Scr.* **2012**, *85*, 035008. [[CrossRef](#)]
15. San, J.Y.; Worek, W.M.; Lavan, Z. Entropy Generation in Convective Heat Transfer and Isothermal Convective Mass Transfer. *J. Heat Transfer* **1987**, *109*, 647–652. [[CrossRef](#)]
16. Tamayol, A.; Hooman, K.; Bahrami, M. Thermal Analysis of Flow in a Porous Medium Over a Permeable Stretching Wall. *Transp. Porous Med.* **2010**, *85*, 661–676. [[CrossRef](#)]
17. Rashidi, M.M.; Ali, M.; Freidoonimehr, N.; Nazari, F. Parametric analysis and optimization of entropy generation in unsteady MHD flow over a stretching rotating disk using artificial neural network and particle swarm optimization algorithm. *Energy* **2013**, *55*, 497–510. [[CrossRef](#)]
18. Shit, G.C.; Haldar, R.; Mandal, S. Entropy generation on MHD flow and convective heat transfer in a porous medium of exponentially stretching surface saturated by nanofluids. *Adv. Powder Technol.* **2017**, *28*, 1519–1530. [[CrossRef](#)]
19. Butt, A.S.; Ali, A. Effects of Magnetic Field on Entropy Generation in Flow and Heat Transfer due to a Radially Stretching Surface. *Chin. Phys. Lett.* **2013**, *30*, 024701. [[CrossRef](#)]

20. Munawar, S.; Ali, A.; Mehmood, A. Thermal analysis of the flow over an oscillatory stretching cylinder. *Phys. Scr.* **2012**, *86*, 065401. [[CrossRef](#)]
21. Khan, M.; Ahmed, J.; Rasheed, Z. Entropy generation analysis for axisymmetric flow of Carreau nanofluid over a radially stretching disk. *Appl. Nanosci.* **2020**, *10*, 5291–5303. [[CrossRef](#)]
22. Choi, S.U.S.; Eastman, J.A. Enhancing thermal conductivity of fluids with nanoparticles. In Proceedings of the International Mechanical Engineering Congress and Exhibition, San Francisco, CA, USA, 12–17 November 1995.
23. Iqbal, K.; Ahmed, J.; Khan, M.; Ahmad, L.; Alghamdi, M. Magnetohydrodynamic thin film deposition of Carreau nanofluid over an unsteady stretching surface. *Appl. Phys. A Mater. Sci. Process.* **2020**, *126*, 105. [[CrossRef](#)]
24. Khan, W.A.; Anjum, N.; Waqas, M.; Abbas, S.Z.; Irfan, M.; Muhammad, T. Impact of stratification phenomena on a nonlinear radiative flow of sutterby nanofluid. *J. Mater. Res. Technol.* **2021**, *15*, 306–314. [[CrossRef](#)]
25. Ali, F.; Ahmad, Z.; Arif, M.; Khan, I.; Nisar, K.S. A Time Fractional Model of Generalized Couette Flow of Couple Stress Nanofluid with Heat and Mass Transfer: Applications in Engine Oil. *IEEE Access* **2020**, *8*, 146944–146966. [[CrossRef](#)]
26. Acharya, N.; Maity, S.; Kundu, P.K. Entropy generation optimization of unsteady radiative hybrid nanofluid flow over a slippery spinning disk. *Proc. Inst. Mech. Eng. Part C J. Mech. Eng. Sci.* **2022**, *09544062211065384*. [[CrossRef](#)]
27. Acharya, N.; Mondal, H.; Kundu, P.K. Spectral approach to study the entropy generation of radiative mixed convective couple stress fluid flow over a permeable stretching cylinder. *Proc. Inst. Mech. Eng. Part C J. Mech. Eng. Sci.* **2021**, *235*, 2692–2704. [[CrossRef](#)]
28. Krishna, M.V.; Chamkha, A.J. Hall and ion slip effects on MHD rotating flow of elastico-viscous fluid through porous medium. *Int. Commun. Heat Mass Transf.* **2020**, *113*, 104494. [[CrossRef](#)]
29. Venkata Ramana, K.; Gangadhar, K.; Kannan, T.; Chamkha, A.J. Cattaneo–Christov heat flux theory on transverse MHD Oldroyd-B liquid over nonlinear stretched flow. *J. Therm. Anal. Calorim.* **2021**, *147*, 2749–2759. [[CrossRef](#)]
30. Al-Mubaddel, F.S.; Farooq, U.; Al-Khaled, K.; Hussain, S.; Khan, S.U.; Ajaz, M.O.; Rahimi-Gorji, M.; Waqas, H. Double stratified analysis for bioconvection radiative flow of Sisko nanofluid with generalized heat/mass fluxes. *Phys. Scr.* **2021**, *96*, 055004. [[CrossRef](#)]
31. Naveen Kumar, R.; Jyothi, A.M.; Alhumade, H.; Gowda, R.J.P.; Alam, M.M.; Ahmad, I.; Gorji, M.R.; Prasannakumara, B.C. Impact of magnetic dipole on thermophoretic particle deposition in the flow of Maxwell fluid over a stretching sheet. *J. Mol. Liq.* **2021**, *334*, 116494. [[CrossRef](#)]
32. Lund, L.A.; Wakif, A.; Omar, Z.; Khan, I.; Animasaun, I.L. Dynamics of water conveying copper and alumina nanomaterials when viscous dissipation and thermal radiation are significant: Single-phase model with multiple solutions. *Math. Methods Appl. Sci.* **2022**. [[CrossRef](#)]
33. Song, Y.-Q.; Waqas, H.; Al-Khaled, K.; Farooq, U.; Gouadria, S.; Imran, M.; Khan, S.U.; Khan, M.I.; Qayyum, S.; Shi, Q.-H. Aspects of thermal diffusivity and melting phenomenon in Carreau nanofluid flow confined by nonlinear stretching cylinder with convective Marangoni boundary constraints. *Math. Comput. Simul.* **2022**, *195*, 138–150. [[CrossRef](#)]
34. Acharya, N.; Mabood, F.; Badruddin, I.A. Thermal performance of unsteady mixed convective Ag/MgO nanohybrid flow near the stagnation point domain of a spinning sphere. *Int. Commun. Heat Mass Transf.* **2022**, *134*, 106019. [[CrossRef](#)]
35. Chamkha, A.J.; Rashad, A.M. Unsteady heat and mass transfer by MHD mixed convection flow from a rotating vertical cone with chemical reaction and Soret and Dufour effects. *Can. J. Chem. Eng.* **2014**, *92*, 758–767. [[CrossRef](#)]
36. Seyed, S.H.; Saray, B.N.; Chamkha, A.J. Heat and mass transfer investigation of MHD Eyring–Powell flow in a stretching channel with chemical reactions. *Phys. A Stat. Mech. Its Appl.* **2020**, *544*, 124109. [[CrossRef](#)]
37. Veera Krishna, M.; Ameer Ahamed, N.; Chamkha, A.J. Hall and ion slip effects on unsteady MHD free convective rotating flow through a saturated porous medium over an exponential accelerated plate. *Alexandria Eng. J.* **2020**, *59*, 565–577. [[CrossRef](#)]
38. Chakraborty, S.; Ray, S. Performance optimisation of laminar fully developed flow through square ducts with rounded corners. *Int. J. Therm. Sci.* **2011**, *50*, 2522–2535. [[CrossRef](#)]
39. Lorenzini, M.; Suzzi, N. The Influence of Geometry on the Thermal Performance of Microchannels in Laminar Flow with Viscous Dissipation. *Heat Transf. Eng.* **2016**, *37*, 1096–1104. [[CrossRef](#)]
40. Lorenzini, M.; Daprà, I.; Scarpi, G. Heat transfer for a Giesekus fluid in a rotating concentric annulus. *Appl. Therm. Eng.* **2017**, *122*, 118–125. [[CrossRef](#)]
41. Coelho, P.M.; Faria, J.C. On the generalized Brinkman number definition and its importance for Bingham fluids. *J. Heat Transfer* **2011**, *133*, 054505. [[CrossRef](#)]